Industrial Crops & Products 226 (2025) 120666

Contents lists available at ScienceDirect

Industrial Crops & Products

journal homepage: www.elsevier.com/locate/indcrop

# Enhanced biodegradability and thermal insulation capability of polylactic acid reinforced with calcium-crosslinked orange peel biochar

Jaeyeon Kim [a], Jaekyung Lee [a], Subin Lee [b], Oju Kwon [a], Jaeho Lee [c], Jooheon Kim [a,b,*]

[a] School of Chemical Engineering, Chung-Ang University, Seoul 06974, Republic of Korea
[b] Department of Intelligent Energy and Industry, Graduate School, Chung-Ang University, Seoul 06974, Republic of Korea
[c] Department of Mechanical and Aerospace Engineering, University of California, Irvine, CA 92679, USA

ARTICLE INFO

*Keywords:*
Flame retardancy
Sodium alginate
Thermal conductivity
Biodegradability
Calcium crosslinking

ABSTRACT

The growing demand for sustainable materials has driven interest in biodegradable polymers such as polylactic acid (PLA). However, PLA's inherent limitations in thermal insulation and flame retardancy restrict its broader applicability. To address these challenges, we produced PLA composites reinforced with various amounts of calcium-crosslinked orange peel biochar (CC-OPB) and discovered that the latter significantly enhanced the thermal and flame-retardant properties of the former. The 6 % CC-OPB/PLA composite achieved the lowest thermal conductivity of 0.081 W/m·K and a V-1 rating in a UL94 plastics flammability standard test. These improvements were attributed to the formation of a protective char layer and enhanced phonon scattering. In addition, the incorporation of CC-OPB accelerated the biodegradation process, with the 6 % CC-OPB/PLA composite showing a weight loss of 25.1 % after 20 days. Our findings demonstrate that CC-OPB/PLA composites offer a promising eco-friendly alternative for industrial applications by imparting superior insulation, fire resistance, and biodegradability to PLA.

## 1. Introduction

The global demand for sustainable materials is rapidly increasing due to environmental issues caused by conventional non-biodegradable plastics. (Asthana et al., 2024; Dananjaya et al., 2024; Zheng et al., 2016) A promising alternative approach is producing bio-based polymers such as PLA from renewable sources such as corn starch. The suitable biodegradable and mechanical properties of PLA have led to it being widely used in packaging and biomedical devices, among other applications. (Hussain et al., 2024; Khouri et al., 2024; Tang et al., 2025; Zhang et al., 2024) However, despite its environmental friendliness, PLA has some limitations such as poor thermal stability and high flammability, which limit its use in demanding manufacturing areas such as automobiles and electronics. To address these limitations, researchers have focused on improving the thermal, mechanical, and flame-retardant properties of PLA by using various fillers. ('Atiqah Abdul Azam et al., 2024; Azka et al., 2024; Liesenfeld et al., 2024) One approach is the use of abundant, cost-effective, and biodegradable bio-fillers such as lignocellulose materials. Not only do these fillers improve the crystallinity and mechanical properties of PLA, but they also contribute to its flame retardancy by forming a differential layer during combustion and enhancing its biodegradability. (Krapež Tomec et al., 2024; Lule and Kim, 2022) In a recent study, Raja and Devarajan (Raja and Devarajan, 2024) investigated the development of biodegradable composites reinforced with flax and basalt fibers, focusing on their potential for thermal insulation in buildings. The composite containing a higher flax fiber ratio achieved a low thermal conductivity of 0.119 W/m·K, indicating excellent thermal insulation performance. These findings suggest that natural fiber-based composites can offer sustainable alternatives to conventional materials for eco-friendly construction.

Agricultural waste materials, especially OPB, show potential as fillers due to their high cellulose content and natural flame-retardant properties. (Alshahrani and Prakash, 2024; Sial et al., 2019) The porous structure of fillers such as OPB promotes microbial colonization, which accelerates the decomposition process. (Chen et al., 2023; Kwon et al., 2019) In addition, surface treatments such as calcium crosslinking further improve the structural stability of PLA and contribute to enhancing its flameproofing and insulation properties. (Aguero et al., 2021; Giz et al., 2020; Tan et al., 2023) Improving the flame resistance of PLA is an important feature for expanding its applicability. Pure PLA is not suitable for high-temperature environments or applications that

* Corresponding author at: School of Chemical Engineering, Chung-Ang University, Seoul 06974, Republic of Korea.
*E-mail address:* jooheonkim@cau.ac.kr (J. Kim).

https://doi.org/10.1016/j.indcrop.2025.120666
Received 26 November 2024; Received in revised form 20 January 2025; Accepted 5 February 2025
Available online 13 February 2025
0926-6690/© 2025 The Authors. Published by Elsevier B.V. This is an open access article under the CC BY-NC-ND license (http://creativecommons.org/licenses/by-nc-nd/4.0/).

require fire resistance because of its high flammability due to its polymer structure. (Zhao et al., 2022; Zhou et al., 2023) However, using fillers such as CC-OPB improves the flame resistance of PLA by improving its self-extinguishing ability and reducing dripping during combustion. The aim of this study is to integrate CC-OPB fillers into PLA to develop biodegradable PLA composites with improved insulation and flame retardancy. (Wu et al., 2023; Zhang et al., 2023) The method used in this study provided CC-OPB/PLA composites with a lower thermal conductivity (0.081 W/mK) and stronger tensile strength (57.3 MPa) compared to conventional filler/PLA-based approaches. Thus, we created a sustainable high-performance composite material suitable for a wide range of industrial applications while focusing on the environmental benefits and the functional enhancements bio-based fillers provide.

### 1.1. Materials

$NH_4OH$ (28–30 %) was purchased from Daejung Chemical and Metals Co., Ltd. (Seoul, Korea), and SA(Sodium Alginate) and $CaCl_2$ were obtained from Sigma-Aldrich (St. Louis, MI, USA). Orange peel was obtained from AMC Allfruit (Australia) and PLA was obtained from Jae Youn Chemical Co., Ltd (Seoul, South Korea). All reactants were used as received without further purification.

### 1.2. Preparation of OPB-$NH_2$

Fresh oranges were initially washed thoroughly to remove any surface impurities and then peeled. The washed OPs were then alternately immersed in liquid nitrogen and deionized water several times, followed by freeze-drying for 72 h to ensure complete dehydration. Following this, the dried OPs were crushed to obtain a fine dry powder, which was then pyrolyzed in a tube furnace at 300 °C under a nitrogen atmosphere for 1 h, resulting in the formation of OPB. To aminate the OPB, 50 ml of $NH_4OH$ was combined with 5 g of OPB and stirred continuously for 24 h. Afterward, the mixture was filtered and thoroughly washed to remove any unreacted reagents and then dried in an oven at 50 °C for 24 h to yield OPB-$NH_2$.

### 1.3. Preparation of CC-OPB

Various weight ratios of OPB-$NH_2$ and SA (1:1, 1:2, or 2:1) were dispersed in deionized water (20 g/L) at 50 °C for 24 h. The resulting SA-OPB mixtures were then centrifuged at 10,000 rpm for 20 min to separate out the precipitate, which was then dried in an oven at 323 K for 24 h. Afterward, the SA-OPB materials were immersed in 0.2 M $CaCl_2$ solution for 2 h to induce calcium crosslinking, resulting in the formation of CC-OPB. Following this, the CC-OPB materials were washed five times with deionized water to remove any residual impurities and then dried overnight in an oven at 50 °C.

### 1.4. Composite preparation via extrusion and injection molding

OPB, CC-OPB, and neat PLA were fed into a twin-screw melt extruder (model BA-11, Bautek, Korea) operating between 170 and 185 °C. During the extrusion process, a vacuum pump was employed to remove vaporized gases and moisture from the screw zones of the extruder. The resulting extrudates were then collected and pelletized at 180 °C using an injection molding machine (BA-915, Bautek, Korea) to form the composites. The component ratios used are detailed in Table S6.

### 1.5. Characterization

Chemical structure analysis was conducted by using FT-IR spectroscopy (ATR mode; Spectrum One, Perkin-Elmer) and XPS (VG Microtech). The crystalline structures of the fillers and matrix were examined via XRD spectroscopy (Bruker-AXS, D8-Advance) at a scan rate of 0.2 $^\circ \cdot s^{-1}$ with Cu Kα radiation (0.154056 nm) in a 2θ range of 10–80°. The morphologies of the composites were investigated using FE-SEM (Sigma, Carl Zeiss). EDS was conducted using a NORAN System 7 instrument (Thermo) at 30 kV to investigate the atomic composition of the fillers. Thermal stability was assessed via TGA (TGA-2050, TA Instruments) while heating a sample to 800 °C at a rate of 20 $^\circ C \cdot min^{-1}$ under a nitrogen atmosphere. The thermal diffusivities of the composites at room temperature were determined by using LFA (NanoFlash LFA 467, Netzsch Instruments Co.). Thermal conductivity (*K*) values (W/m•K) were calculated using the following formula:

$$K = \alpha \times \rho \times Cp,$$

where α denotes the thermal diffusivity ($mm^2/s$), ρ signifies the bulk density ($g/cm^3$), and *Cp* stands for the room-temperature heat capacity (J/g•K). Electrical conductivity values were determined by using the four-point probe method. Tensile strength was assessed by utilizing a universal testing machine (UTM-301, R&B Corp., Daejeon, Korea) at room temperature with a crosshead speed of 5 mm/min, a tension loading rate of 10 mm/min, and a load force of 100 kg/mm. The flammability of the composites with respect to the UL94 plastics flammability standard was investigated by directly applying a flame to a sample for 10 s twice. Biodegradation tests of samples were referred to the ASTM D5338 standard. Samples were cut into 2.8 mm diameter circle and weighed. Compost media were prepared in plastic containers with a thickness of 20 cm, and the samples were buried up to 10 cm deep in the media. To ensure moisture retention, the medium was sprayed twice daily. After 20 days, the films were extracted from the media, cleaned, disinfected in 70 % ethanol, and dried in an oven at 50 °C for 24 hours. The weight loss of the samples due to biodegradation was calculated using the formula:

$$\text{Weight loss} = (W_0 - W_A) / W_0 \times 100\%,$$

where $W_0$ and $W_A$ are the weight of the initial sample and the weight of the sample after biodegradation over a certain time period.

## 2. Results and discussion

### 2.1. Chemical characterization of the composites

The fabrication processes for the fillers and composites are shown schematically in Fig. 1. Fig. 2(a-c) depicts the SEM images of OP (a), OPB (b), and OPB-$NH_2$ (c). The SEM image of OP shows that the material has an uneven, relatively smooth structure typical of lignocellulosic materials like orange peel, which retains the structural integrity of cellulose, hemicellulose, and lignin. The surface is primarily intact, showing minimal texture. Upon pyrolysis, OP transforms into OPB, exhibiting a notably rougher surface and a significantly larger surface area. While no distinct porous structure is visible, the increased surface roughness is attributed to the decomposition of organic matter at high temperatures. During pyrolysis, volatile compounds are released, leading to a more textured carbon matrix. These changes result in defects and structural roughness, which are advantageous for improving the thermal insulation properties due to the increased surface area that helps reduce thermal conductivity. (Amin et al., 2019) The rough texture of OPB makes it suitable as a thermal filler, enhancing the material's ability to trap heat and act as a thermal insulator. Further modification of OPB to OPB-$NH_2$ through surface amination introduces more visible defects and etching on the biochar surface, leading to additional roughness and textural irregularities. These defects increase the interaction between the biochar and SA. The increased defects and surface area contribute to its functionality as a thermal insulation filler by further lowering thermal conductivity, which is essential for enhancing the thermal performance of composites. Fig. 2(d–i) depicts SEM and EDS mapping images of SA-OPB and CC-OPB. The SEM image of SA-OPB in Fig. 2(d) showed a smoother and more uniform surface compared to OPB-$NH_2$, suggesting that SA formed a consistent coating over the biochar particles. EDS

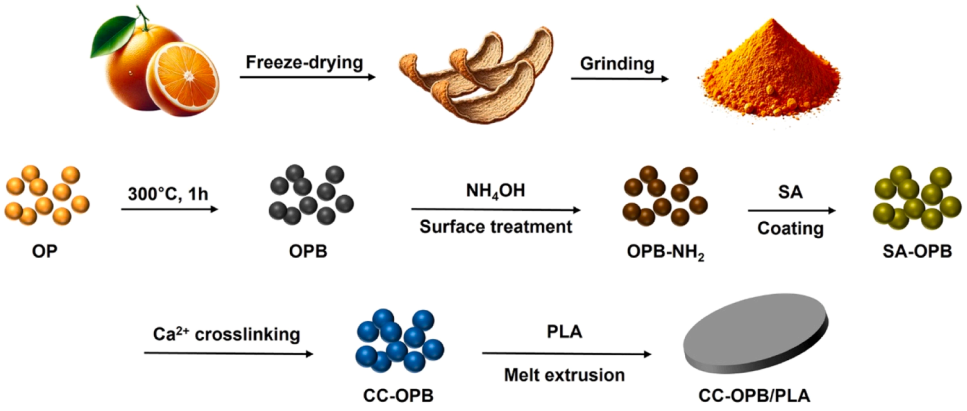



**Fig. 1.** Schematic illustration of the composites fabrication process.

analysis showing the presence of Na and O in Fig. 2(f) confirms this finding. After immersing SA-OPB in $CaCl_2$ to induce calcium crosslinking, the SEM image of CC-OPB in Fig. 2(g) shows a more structured and rigid surface, thereby confirming successful crosslinking. The EDS image in Fig. 2(h) reveals the presence of Ca in CC-OPB, thus confirming the introduction and integration of Ca ions. The formation of CC networks with SA is essential for improving the structural stability of the complex.(Choi et al., 2022)

XRD analysis was performed to examine the crystalline structures of OP, OPB, SA-OPB, and CC-OPB in Fig. 3(a). The XRD pattern for OP show peaks at 15.6° and 22.1°, which is characteristic of semi-crystalline cellulose. (Praipipat et al., 2023) After pyrolysis, the XRD pattern for OPB shows a wide peak around 24° indicating a disordered carbon structure and amorphous carbon formation. The pyrolysis process removed the crystalline cellulose component and created a more amorphous and carbon-rich structure. (Xue et al., 2024) The XRD pattern for SA-OPB shows new peaks at around 13° and 20° corresponding to SA, thereby indicating the semi-crystalline nature of SA-OPB. This result indicates that SA improved the mechanical properties of the material by forming a semi-crystalline structure on the OPB-$NH_2$ surface. The XRD pattern for CC-OPB after calcium crosslinking indicates that the intensity of the peak at 20° increased, thereby signifying improved structural order due to the formation of a CC network. This increase in crystallinity suggests that the calcium crosslinking process improved the structural stability of the composite material. (Urquiza et al., 2011)

Fig. 3(b) illustrates TGA curves for OP, OPB, SA-OPB, and CC-OPB. The curve for dried OP shows three main steps of weight loss. The first step between 50 and 150 °C is due to water evaporation. The second step shows major weight loss occurring between 200 and 350 °C due to the degradation of hemicellulose and cellulose. In the third step, lignin degradation occurred between 350 and 500 °C, resulting in slower progressive weight loss due to destruction of the complex aromatic structure. Thus, OP shows significant thermal instability, with the decomposition of most of the organic content at relatively low temperatures. In contrast, OPB was much more thermally stable. After the initial water loss, primary decomposition occurred between 300 and 600 °C, reflecting the decomposition of residual carbonaceous materials that had not been completely converted during the pyrolysis process. Above 600 °C, OPB exhibited minimal weight loss, thereby indicating the formation of a stable carbon matrix with strong resistance to further pyrolysis. The TGA curve for SA-OPB shows increased weight loss below 150 °C due to the hydrophilic nature of sodium alginate (SA), which retains more moisture compared to OPB. Between 200 and 350 °C, the curves for OPB and SA-OPB are parallel, indicating no distinct additional degradation step due to SA. Above 350 °C, the thermal stability of SA-OPB is enhanced, likely due to the formation of a stable char layer. The TGA curve for CC-OPB shows slightly improved thermal stability compared to SA-OPB. The decomposition of CC-alginate began at higher temperatures, indicating that the presence of Ca ions enhances the thermal resistance of the alginate network. Moreover, CC-OPB was stable above 350 °C.

FT-IR spectra for OP, OPB, OPB-$NH_2$, SA-OPB, and CC-OPB are depicted in Fig. 3(c-d). The FT-IR spectrum for dried OP shows characteristic peaks at 3287 $cm^{-1}$ for O-H stretching vibrations, 2923 $cm^{-1}$ for C-H stretching, 1735 $cm^{-1}$ for C═O stretching in the carbonyl group, 1605 $cm^{-1}$ for C═C stretching in the lignin aromatic ring, and 1021 cm-1 for C-O-C stretching in the ether group.(Terzioğlu et al., 2021) After the formation of OPB via pyrolysis, the peaks associated with oxygen-containing functional groups O-H stretching (3287 $cm^{-1}$) and C═O stretching (1735 $cm^{-1}$) decreased, resulting in the elimination of hydrophilicity and the formation of a more aromatic structure evidenced by the peak at 1591 $cm^{-1}$ (C═C-C aromatic ring stretching) becoming predominant.(Moradi-Choghamarani et al., 2019) The addition of amine groups to produce OPB-$NH_2$ resulted in new peaks corresponding to N-H bending and C-N stretching vibrations at 1571 and 1377 $cm^{-1}$ , respectively, in its FT-IR spectrum.(Xue et al., 2024) These peaks confirm the successful introduction of amine groups that enhance the chemical reactivity of the biochar surface. The FT-IR spectrum for SA-OPB shows additional peaks corresponding to the carboxylate salt groups: symmetric and asymmetric $–COO^-$ stretching vibration peaks at 1587 and 1376 $cm^{-1}$, thereby confirming the presence of SA on the OPB surface. Moreover, the N-H and C-N peaks of OPB-$NH_2$ were still present but had migrated slightly, indicating the interaction between the amine group and SA. The FT-IR spectrum for CC-OPB showed a shift in the peak at 1598 and 1390 $cm^{-1}$ due to carboxylate, thus confirming interactions between Ca ions and the carboxylate group in alginate. (Yu et al., 2021; Zheng et al., 2016)

Fig. 4 illustrates XPS spectra for OP, OPB, OPB-$NH_2$, SA-OPB, and CC-OPB. The deconvoluted C 1 s spectrum for OP in Fig. 4(a) shows peaks at 284.73 eV (C-C/C-H), 286.56 eV (C-O), and 288.56 eV (O-C═O). (Wang et al., 2022) These peaks were significantly reduced in the C 1 s spectrum for OPB in Fig. 4(b), reflecting the loss of oxygenating functional groups during pyrolysis and an increase in graphite carbon content. In the C 1 s spectrum for OPB-$NH_2$ in Fig. 4(c), a new peak appeared at 285.8 eV, confirming the incorporation of nitrogen into the biochar matrix due to C-N binding. The O 1 s spectrum for OP in Fig. 4 (d) reveals peaks at 531.27 eV (C═O) and 533.09 eV (C-OH/C-O-C). The N 1 s spectrum for OPB-$NH_2$ in Fig. 4(e) shows three deconvoluted peaks at 398.53 eV, 399.90 eV, and 401.61 eV corresponding to pyridine-N, pyrrolic-N, and graphite-N or oxidative-N, respectively, thus confirming the successful amination of the biochar surface. (Narukulla et al., 2022) The XPS spectrum of SA-OPB in Fig. 4(f) reveals an additional Na 1 s peak at 1071.5 eV. Meanwhile, in Fig. 4(g), the intensity of the C-O and O-C═O peaks increases due to the carboxyl and hydroxyl groups of the alginate moiety, resulting in the appearance of an

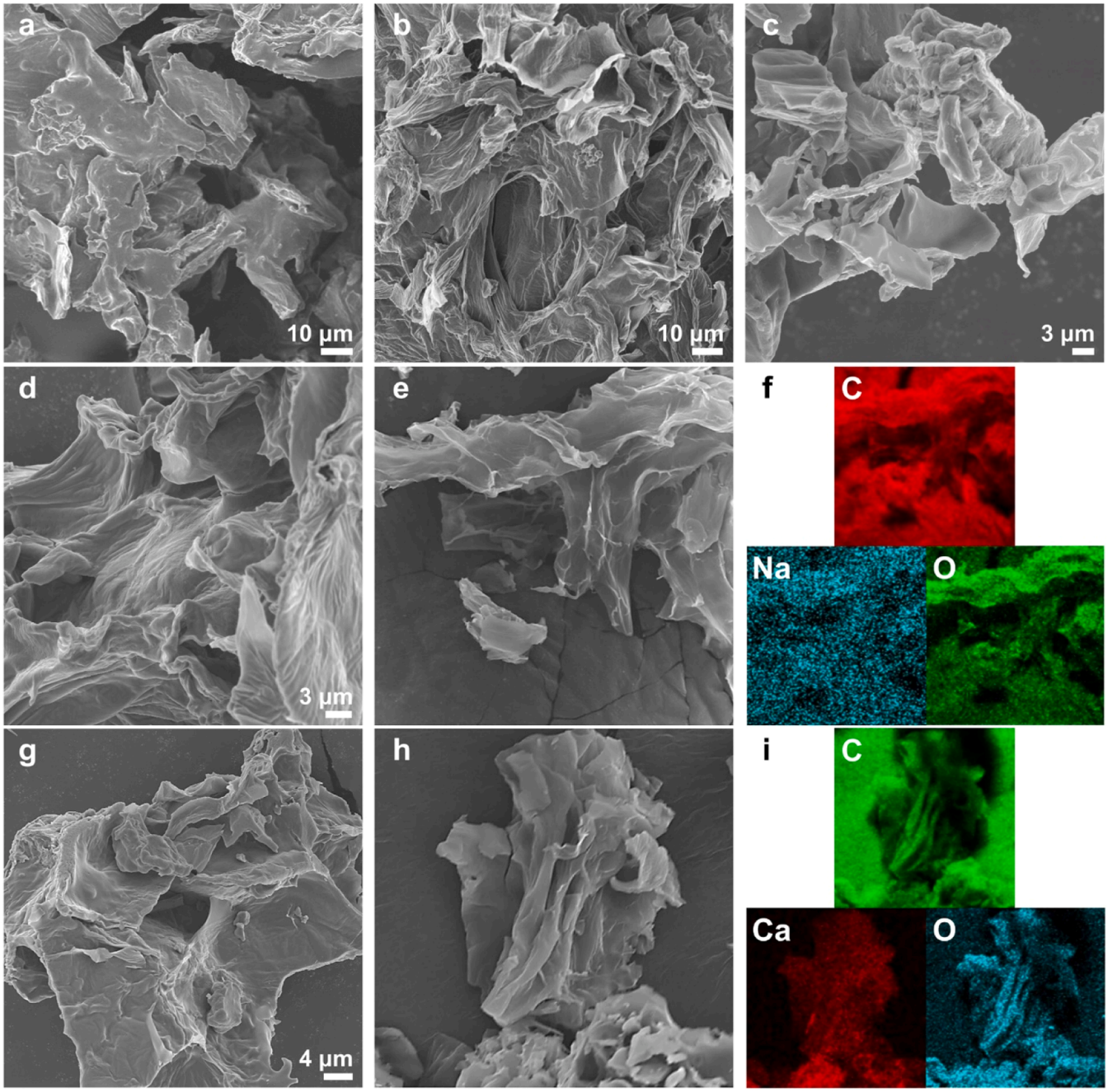



**Fig. 2.** FE-SEM images of (a) OP, (b) OPB, (c) OPB-$NH_2$, (d) SA-OPB and (e) CC-OPB. EDS elemental mapping of (f-g) SA-OPB and (h-i) CC-OPB.

additional C═O peak at 287.80 eV. These changes confirm that SA was successfully coated on the OPB-$NH_2$ surface. In the XPS spectra for CC-OPB in Fig. 4(h), Ca $2p_{1/2}$ and Ca $2p_{3/2}$ peaks with binding energies of 347.73 eV and 351.29 eV confirm the presence of Ca ions and successful calcium crosslinking. The O 1 s spectrum for CC-OPB in Fig. 4(i) contains a peak at 532.50 eV reflecting the formation of Ca-O bonds, thereby further confirming the generation of CC-alginate structures. In addition, the (C-OH/C-O-C) and (C═O) peaks of O 1 s were shifted to higher energies, respectively. This can be attributed to the reduction of the electron density around the oxygen by redistributing the electron density by the binding of $Ca^{2+}$ ions to the oxygen in the alginate. (Song et al., 2023)

### 2.2. Morphological analysis of the composites

The SEM image of neat PLA in Fig. 5(a) shows that it has a smooth surface. The SEM image of 4 % OPB/PLA in Fig. 5(b) exhibits voids between the filler particles and the PLA matrix, thus inferring weak interfacial bonding. Although the air within these voids has low thermal conductivity, the inconsistent distribution of OPB and loose filler-matrix interface reduce the overall structural integrity and mechanical properties of the composite. While air gaps can contribute to insulation, unregulated voids still create pathways for local heat bridges to form, resulting in uneven heat transfer. The SEM images of the CC-OPB/PLA composites in Fig. 5(c–f) show a much more uniform distribution of filler particles with smaller voids and stronger filler-matrix adhesion. This enhanced bonding reduces the likelihood of forming large unstructured voids that can lead to inefficient heat transfer. Here, the

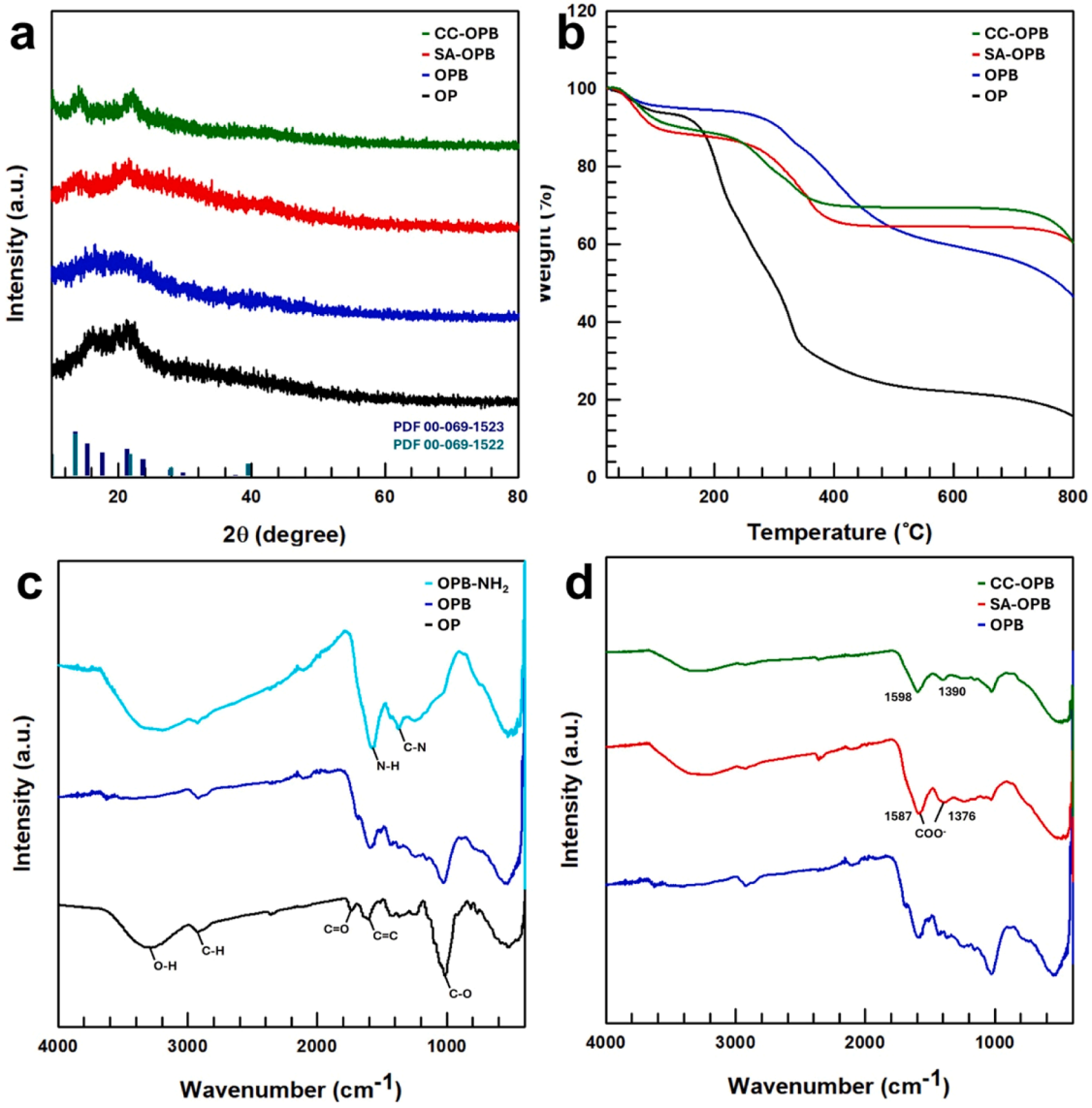



**Fig. 3.** (a) XRD patterns of fillers. (b) TGA graphs of fillers. FT-IR of (c) OP, OPB, and OPBNH₂. (d) SA-OPB and CC-OPB.

smaller voids and stronger interfacial connection between the filler particles and PLA help scatter heat transfer phonons more effectively than in OPB/PLA. Moreover, the presence of the SA coating and CC structures in CC-OPB/PLA further enhance phonon scattering, especially at the interface between the filler and the matrix. Since phonon scattering interferes with the transfer of heat through a material, it is very important to lower the thermal conductivity. CC-alginate not only improved the mechanical strength of the composites, it also created an additional barrier for phonon propagation, thus contributing to a more heat-resistant structure.

### 2.3. *Thermal Properties of the Composites*

The thermal conductivity analysis results for 6 % CC-OPB/PLA, 4 % CC-OPB/PLA, and 2 % CC-OPB/PLA in Fig. 6(a) indicate that the thermal conductivity decreased as the CC-OPB filler content was increased (0.087, 0.092, and 0.113 W/m·K, respectively). Furthermore, that of 4 % OPB/PLA was 0.145 W/m·K while that of neat PLA was the highest at 0.278 W/m·K. The main factors influencing the thermal conductivity as the CC-OPB content was increased are the porosity and low intrinsic thermal conductivity of the filler. CC-OPB contains a CC-alginate network, leading to numerous pores filled with air and making the composites poor heat conductors. These air pockets act as a barrier to heat transfer by extending the conduction path and reducing the overall heat flow through the composite material. As the filler content was increased, the number of pores increased, which further reduced the thermal conductivity. Furthermore, the introduction of SA coating and calcium crosslinking not only improved filler-matrix bonding but also created additional interfaces that scatter phonons, thereby further disrupting the efficient transfer of heat. This scattering effect is especially pronounced in the composite with the highest filler concentration. In contrast, the weak interface between the filler and PLA in OPB/PLA reduces the opportunity for phonon scattering. (Díez-García et al., 2020; Jin et al., 2023; Yan et al., 2023) The thermal conductivity values for CC-OPB/PLA composites with sodium alginate (SA) to OPB-NH₂ weight ratios of 2:1, 1:1, or 1:2 were 0.097, 0.087, and 0.081 W/m·K, respectively (Fig. 6(b)). This trend of decreasing thermal conductivity with an increased amount of SA is attributed to OPB having naturally lower thermal conductivity and a more highly porous structure than SA. Since the rough, irregular surfaces of the biochar particles break the coherent flow of phonons, a higher concentration of OPB makes phonon scattering more pronounced at the filler-matrix interface.

Details regarding the thermal conductivity of the composites are summarized in Table S2 and S3. Fig. 9(c) presents the results of fitting

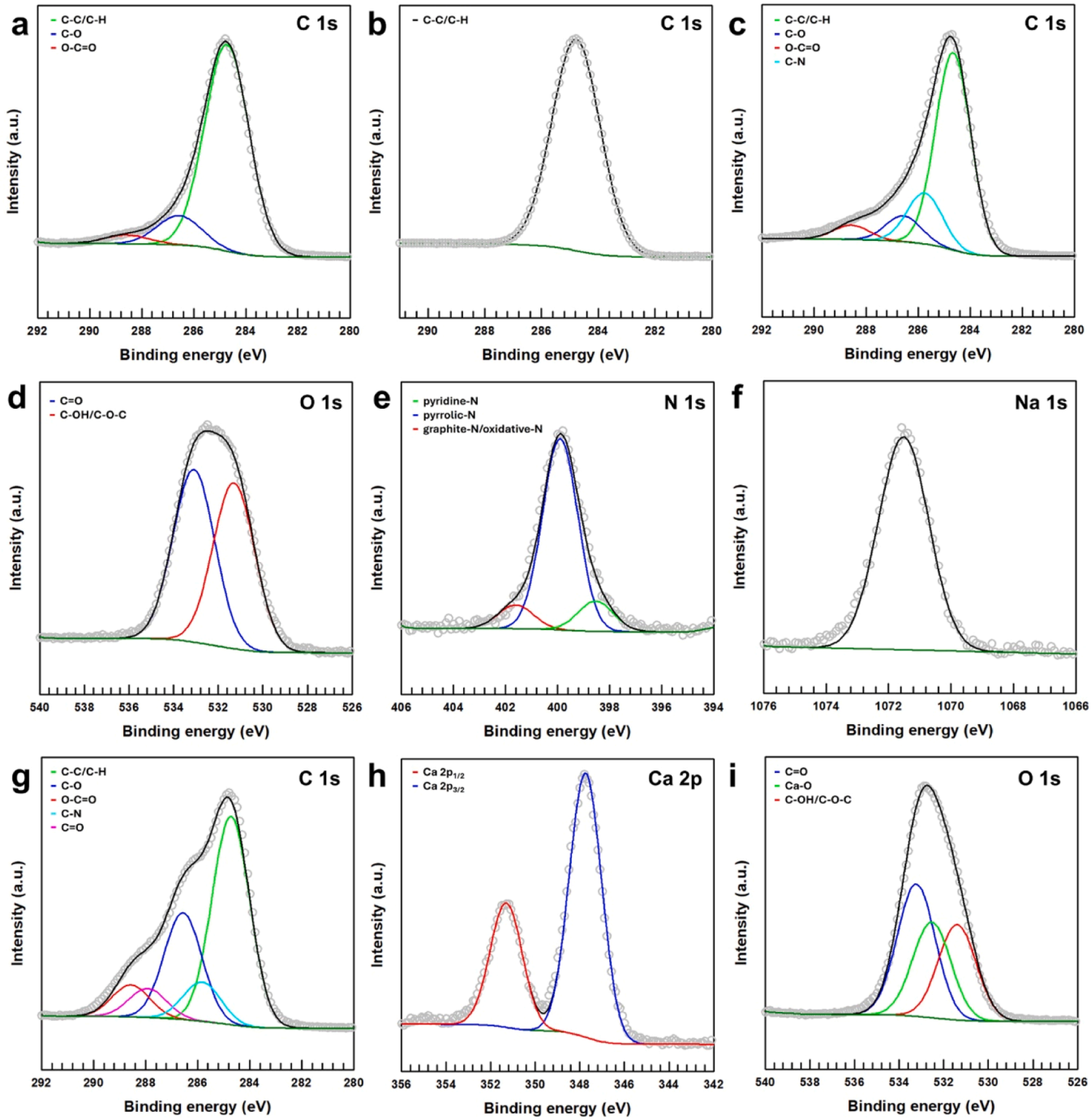



**Fig. 4.** XPS data of (a) OP C 1 s, (b) OPB C 1 s, (c) OPB-$NH_2$ C 1 s, (d) OP O 1 s, (e) OPB-$NH_2$ N 1 s, (f) SA-OPB Na 1 s, (g) SA-OPB C 1 s, (h) CC-OPB Ca 2p, (i) CC-OPB O 1 s.

thermal conductivity using the Agari–Uno model. We employed the Agari–Uno model, which considers the formation of thermal conduction pathways. The experimental values matched well with the theoretical values from the model. We proceeded with modeling via fitting, substitution, and logarithm processes. Details of the Agari–Uno model fitting process are discussed in the Supporting Information.

The images in Figs. 7(a) and 7(b) display the composites after exposure to a flame. The flame retardancy of the composites rated using the UL94 vertical combustion test resulted in 6 % CC-OPB/PLA being V-0; 4 % CC-OPB/PLA, 2 % CC-OPB/PLA, 4 % OPB/PLA, and neat PLA being V-1. The weight loss data following the fire test have been summarized in Table 1. These results highlight a significant improvement in the flame retardancy achieved by incorporating CC-OPB filler into the PLA matrix. The V-0 grade achieved by 6 % CC-OPB/PLA indicates that it can delay flame propagation and reduce the post-flame time. In this case, the composites self-extinguished within 10 seconds after the flame was removed, and no combustion droplets were observed. This enhanced flame retardancy can be attributed to several factors related to the structure and composition of the CC-OPB filler. The porous structure of the CC-OPB filler formed during the pyrolysis process creates a thermal barrier by trapping air and other gases within micropores and nanopores. These trapped gases reduce heat transfer to the PLA matrix, which slows down the combustion process. In addition, calcium cross-linking in CC-OPB can act as a physical barrier to protect the underlying

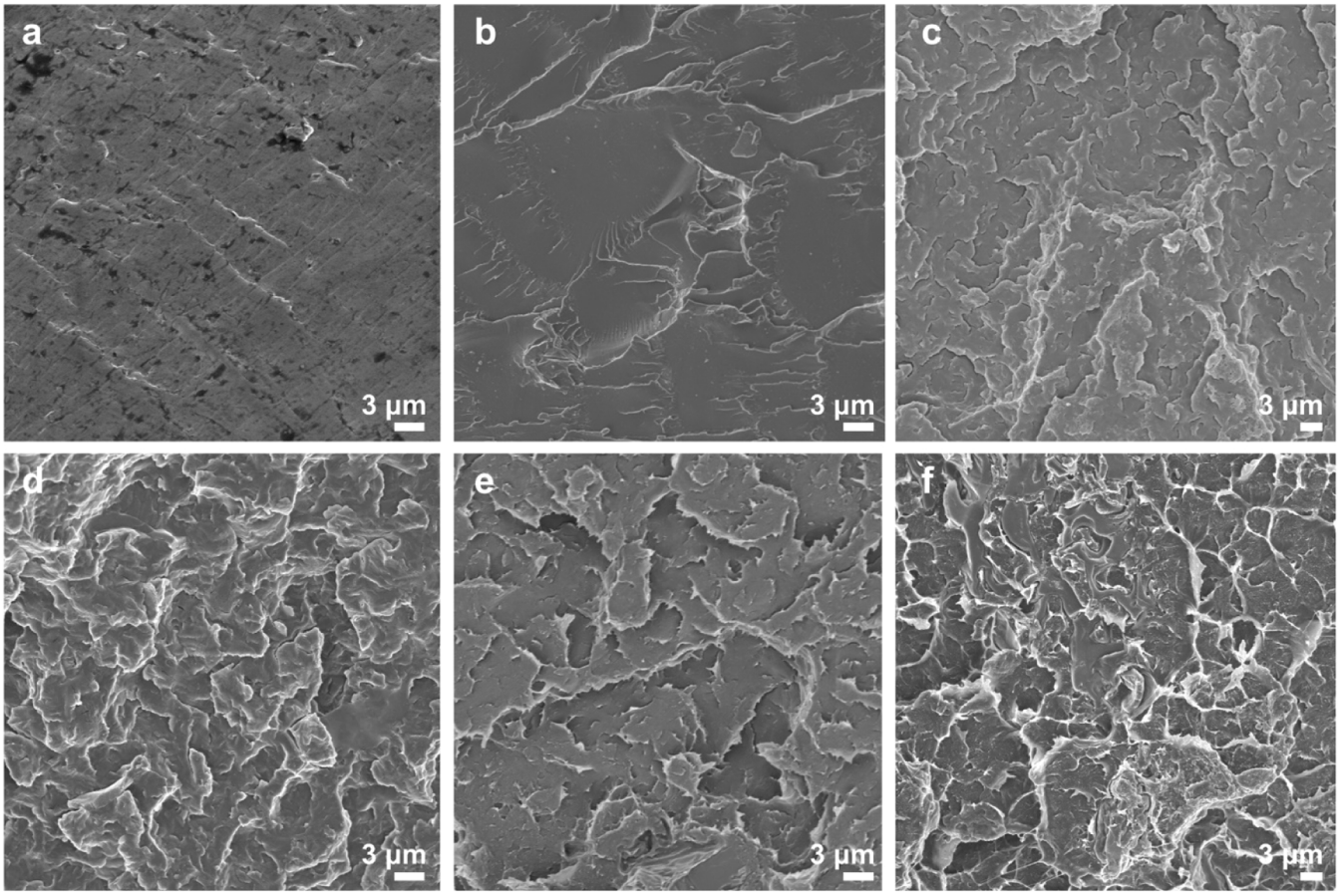



**Fig. 5.** FE-SEM images of (a) neat PLA, (b) 4 % OPB/PLA, (c) 1 % CC-OPB/PLA, (d) 2 % CC-OPB/PLA, (e) 4 % CC-OPB/PLA, (f) 6 % CC-OPB/PLA.

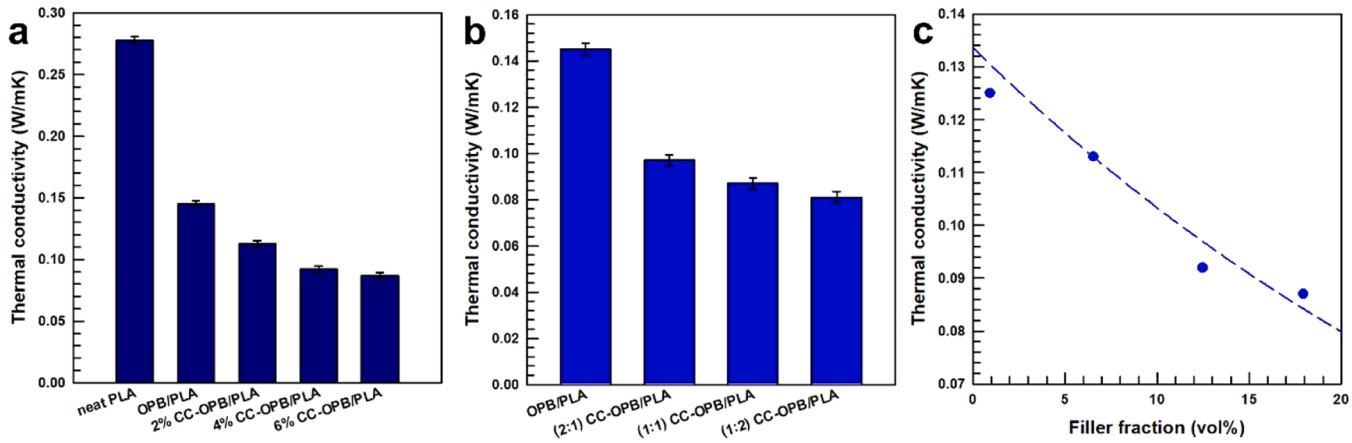



**Fig. 6.** (a) Thermal conductivity of composites, (b) thermal conductivity of composites in filler ratios, (c) theoretical thermal conductivity values obtained from the Agari–Uno model.

material from heat and oxygen exposure by promoting the formation of a differential layer during combustion. (Li et al., 2022) The formation of this protective barrier layer is a key mechanism of flame retardancy because it not only insulates the material but also limits the release of volatile combustible gases that can otherwise supply the flame. The detailed XRD patterns of the residual char are provided in Fig. S3 of the Supporting Information. In contrast, the 4 % CC-OPB/PLA composite received a lower UL94 grade (V-1), indicating that it exhibited some flame resistance but did not prevent flame droplets from forming during testing. Thus, the lower concentration of CC-OPB was less effective at protecting the PLA layers.

### 2.4. Mechanical properties of the composites

Fig. 8(a) illustrates tensile stress-strain curves for the materials: neat PLA showed the highest tensile strength (85.1 MPa), followed by 6 % CC-OPB/PLA (52.6 MPa), 4 % CC-OPB/PLA (42.5 MPa), 2 % CC-OPB/PLA (23.2 MPa), and 4 % OPB/PLA (10.3 MPa) while their elongation at break values were 6.9 %, 5.7 %, 4.5 %, 3.7 %, and 1.8 %, respectively. The good tensile strength of pristine PLA is mainly due to its

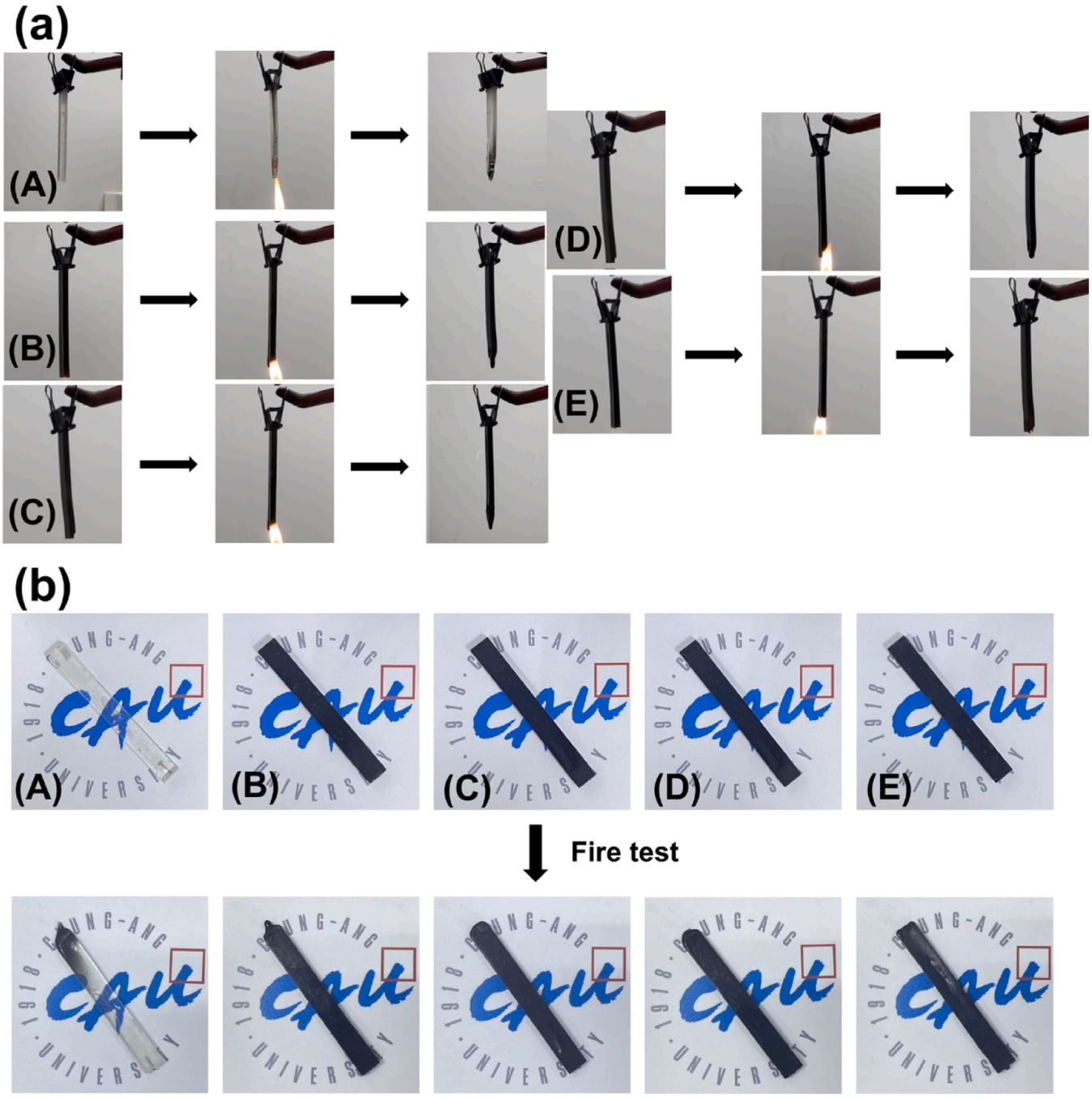



**Fig. 7.** (a) Fire test images of composites. (b) Images of composites before and after fire test. ((A) neat PLA, (B) 4 % OPB/PLA, (C) 2 % CCOPB/PLA, (D) 4 % CC-OPB/PLA, (E) 6 % CC-OPB/PLA.

**Table 1**
Weight loss of composites after fire test.

| Composite | Weight loss (%) |
|---|---|
| neat PLA | 13.2 |
| 4 % OPB/PLA | 7.8 |
| 2 % CC-OPB/PLA | 5.2 |
| 4 % CC-OPB/PLA | 2.3 |
| 6 % (1:1) CC-OPB/PLA | 1.1 |

uniform structure, which enables a uniform load distribution throughout the matrix, thereby minimizing the stress concentration that can lead to cracking. Among the composites, 6 % CC-OPB/PLA showed the highest tensile strength (52.6 MPa) and elongation at break (5.7 %). Thus, the higher the CC-OPB content, the greater the interaction between the filler and the matrix providing better reinforcement. Lowering the CC-OPB content reduced the interaction between the filler and the matrix, leading to less effective stress transfer and reducing both strength and ductility. The 4 % OPB/PLA composite showed the lowest tensile strength (10.3 MPa) and elongation at break (2.3 %), which is probably due to the interfacial bonding between the OPB filler and the PLA matrix being weak without the addition of SA. (Wang et al., 2021)

Fig. 8(b) demonstrates the effect of filler composition on the tensile strength and elongation at breakage of the CC-OPB composites with an SA ratio of 2:1, 1:1, or 1:2: their tensile strength values were 57.3, 52.6, and 47.2 while their elongation at break values were 5.9 %, 5.7 %, and

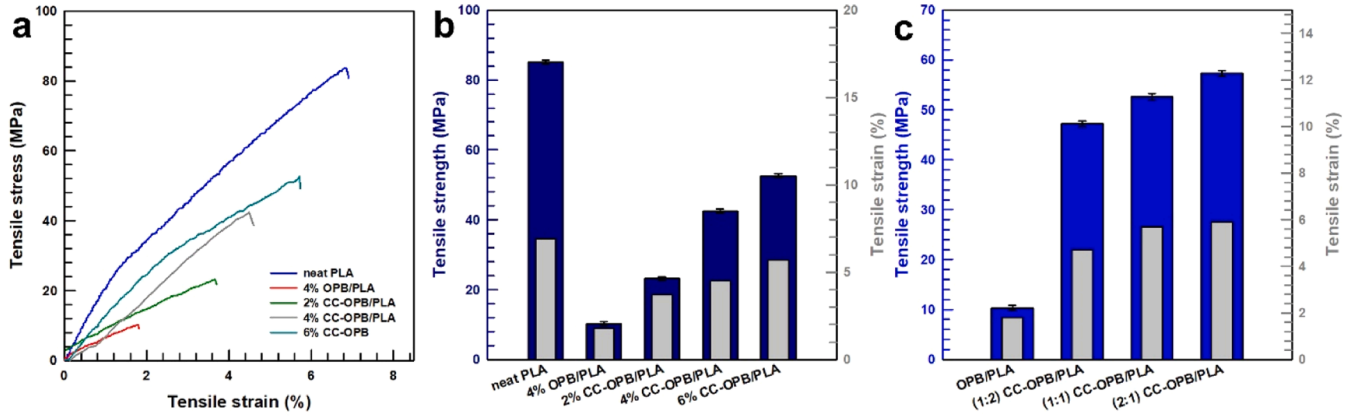



**Fig. 8.** (a) Stress-Strain curve of composites. (b) Tensile strength and strain of composites. (c) Stress-Strain curve of composites in filler ratios.

4.7 %, respectively. These results indicate that the tensile strength and elongation at break slightly decreased as the proportion of SA was increased. This could be due to the higher OPB content causing more discontinuity in the matrix and reducing the flexibility of the composite.

### 2.5. Biodegradability of the composites

Fig. 9(a) shows the results of biodegradability testing of OPB/PLA and CC-OPB/PLA over 20 days. The 6 % CC-OPB/PLA composite showed the highest weight loss rate of 25.1 %, followed by 4 % CC-OPB/PLA (21.1 %), 2 % CC-OPB/PLA (18.2 %), 4 % OPB/PLA (11.2 %), and pristine PLA (2.1 %). These results indicate that the incorporation of the CC-OPB filler into PLA significantly improves the biodegradation of the latter, as reflected by the increase in weight loss. This trend is due to the structural and chemical properties of CC-OPB and its interaction with the PLA matrix. CC-OPB was isolated from bio-based material OPB and treated with natural polysaccharide SA, both of which are biodegradable. The porous structure of CC-OPB formed during the pyrolysis process of OP and subsequent SA coating and calcium crosslinking promotes microbial colonization by providing various sites for enzyme adsorption and microbial growth. (Omura et al., 2024) The high porosity and large surface area enhance the decomposition process as microorganisms could more easily penetrate the complex and consume the bio-filler materials. The highest weight loss observed for the 6 % CC-OPB/PLA composite was due to it having the highest filler content. In addition, calcium crosslinking in CC-OPB provides structural stability and does not inhibit biodegradation. Instead, the CC-alginate network allows water and microbial enzymes to penetrate the PLA matrix, thus facilitating the degradation of the composite. SA in CC-OPB is known to be hydrophilic, thereby further accelerating the degradation process by promoting water absorption and creating an environment favorable for microbial activity. The 4 % CC-OPB/PLA and 2 % CC-OPB/PLA composites also showed significant weight loss, albeit lower than that of the 6 % CC-OPB/PLA composite. This reduction in biodegradation can be explained by the reduced accessibility to the PLA matrix for microbial attack due to the lower CC-OPB content. On the other hand, the 4 % OPB/PLA composite showed lower weight loss than the CC-OPB composites, likely due to the lack of SA coating and calcium crosslinking. No SA treatment means that the OPB particles were less hydrophilic, and thus could not absorb water as effectively as CC-OPB, resulting in a

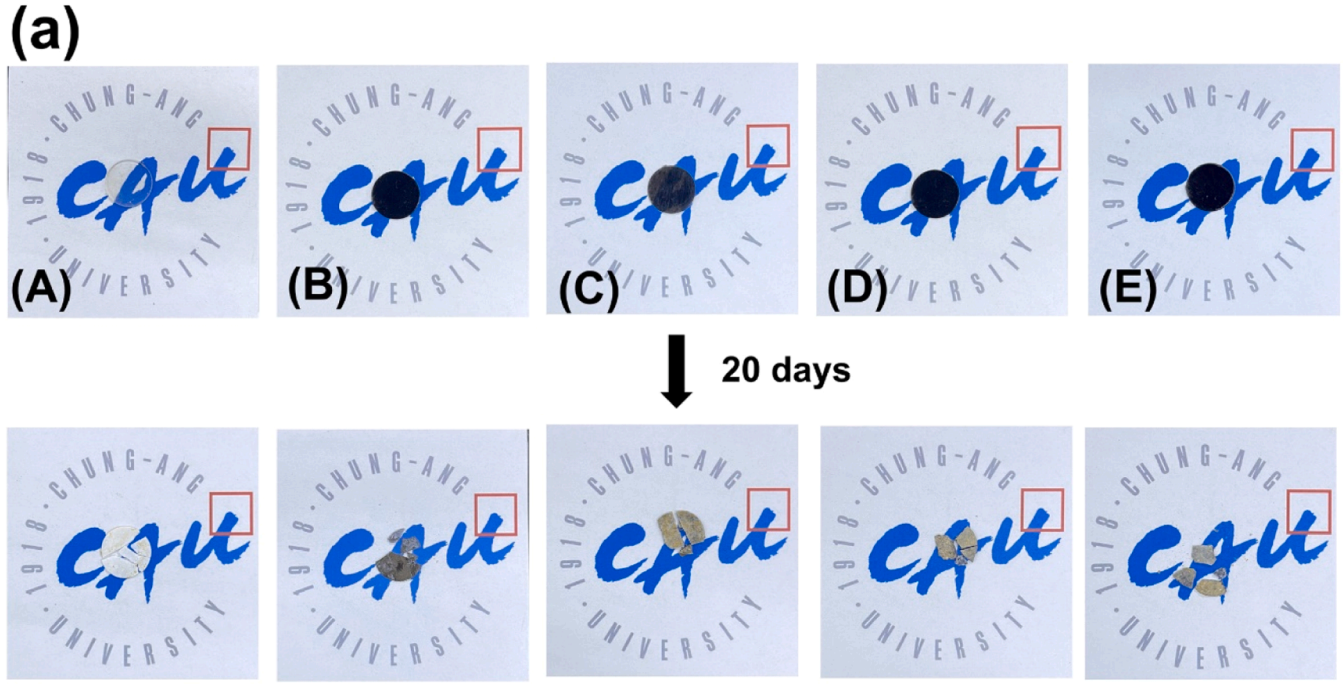



**Fig. 9.** (a) Biodegradability test images of composites. ((A) neat PLA, (B) 4 % OPB/PLA, (C) 2 % CCOPB/PLA, (D) 4 % CC-OPB/PLA, (E) 6 % CC-OPB/PLA.

slower biodegradation rate by limiting microbial colonization and enzymatic activity.

The biodegradation of PLA composites is primarily facilitated by microbial enzymes such as lipases and esterases, which hydrolyze the ester bonds in PLA. The incorporation of CC-OPB enhances this process by increasing the composite's porosity and surface area, promoting water penetration and enzyme-substrate interactions. Furthermore, the calcium alginate network within CC-OPB acts as a scaffold, creating a conducive environment for microbial colonization and enzymatic activity. Previous studies have demonstrated the effectiveness of such biopolymer scaffolds in stabilizing enzymes and enhancing microbial interactions in composite systems. (Xiang et al., 2023; Xu et al., 2021) The increased surface roughness and porosity observed in SEM images further suggest that CC-OPB supports microbial colonization and facilitates enzymatic degradation.

To investigate the biodegradation behavior, SEM analysis was performed on PLA and its composites with OPB and CC-OPB after degradation. As shown in Fig. 10, the SEM image of PLA (Fig. 10a) indicates a relatively smooth surface with minimal signs of degradation. For OPB/PLA (Fig. 10b), small pores and surface roughness appear due to partial hydrolysis of the PLA matrix. With the addition of CC-OPB, the composites (Figs. 10c–10e) show an increasing degree of porosity and surface roughness proportional to the filler content. In particular, the 6 % CC-OPB/PLA sample (Fig. 10e) exhibits significant structural disruption, consistent with extensive hydrolysis. These results suggest that the degradation pathway involves hydrolysis of ester bonds in PLA, leading to the formation of oligomers and monomers. Furthermore, the increased porosity aligns with the hypothesis that the interactions between the PLA matrix and CC-OPB filler enhance biodegradation by facilitating water penetration and catalytic activity.

## 3. Conclusions

We successfully improved the biodegradability, thermal insulation capability, and flame retardancy of PLA by incorporating a CC-OPB filler into its matrix. The addition of CC-OPB also significantly reduced the thermal conductivity of PLA, with the lowest value of 0.081 W/m·K observed for the composite with a 1:2 SA-OPB ratio, likely due to its highly porous structure and improved phonon scattering at the filler-matrix interface. The 6 % CC-OPB/PLA composite achieved a V-1 rating in the UL94 test, thereby confirming the improvement in flame retardancy over PLA. This was attributed to the formation of a protective char layer in OPB facilitated by calcium crosslinking and SA slowing down combustion and reducing flammable gas release. Biodegradation testing revealed that the CC-OPB/PLA composites exhibited higher weight loss compared to neat PLA over time, with 6 % CC-OPB/PLA showing the highest rate at 25.1 % after 20 days. The filler's bio-based nature and porous structure promoted microbial colonization, thereby accelerating degradation.

Overall, the incorporation of the CC-OPB filler not only significantly enhanced the thermal and flame-retardant properties of PLA but also greatly improved its biodegradability. These findings demonstrate the potential of CC-OPB as an effective bio-filler for developing high-performance, eco-friendly PLA-based composites. The superior thermal insulation, fire resistance, and biodegradation of CC-OPB/PLA composites over PLA offer a compelling solution for industries seeking sustainable materials that meet both environmental and safety standards.

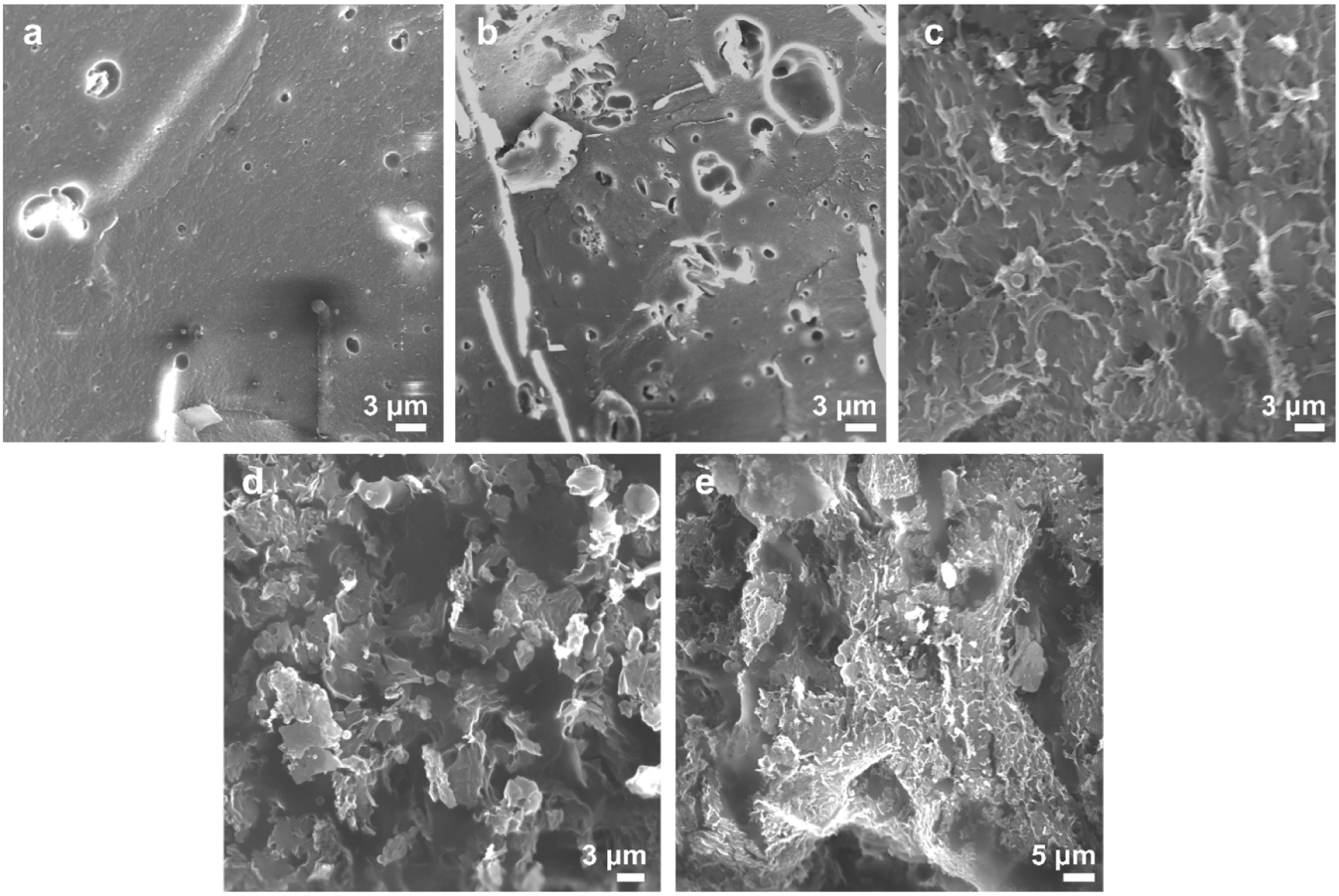



**Fig. 10.** SEM images of PLA and its composites after biodegradation: (a) PLA, (b) OPB/PLA, (c) 2 % CC-OPB/PLA, (d) 4 % CC-OPB/PLA, and (e) 6 % CC-OPB/PLA.

## CRediT authorship contribution statement

**Kim Jooheon:** Supervision, Project administration, Funding acquisition. **Lee Jaeho:** Supervision, Project administration. **Lee Jaekyung:** Formal analysis, Data curation. **Lee Subin:** Formal analysis, Data curation. **Kwon Oju:** Formal analysis, Data curation. **Kim Jaeyeon:** Writing – original draft, Methodology, Investigation, Formal analysis, Data curation, Conceptualization.

## Declaration of Competing Interest

The authors declare that they have no known competing financial interests or personal relationships that could have appeared to influence the work reported in this paper.

## Acknowledgements

This research was funded and conducted under the Competency Development Program for Industry Specialists of the Korean Ministry of Trade, Industry and Energy (MOTIE), operated by Korea Institute for Advancement of Technology (KIAT). (No. P0012453, Next-generation Display Expert Training Project for Innovation Process and supported by the National Research Foundation of Korea (NRF) grant funded by the Korea government (MSIT) (RS-2024-00350658).

## Appendix A. Supporting information

Supplementary data associated with this article can be found in the online version at doi:10.1016/j.indcrop.2025.120666.

## Data availability

The authors are unable or have chosen not to specify which data has been used.

## References

'Atiqah Abdul Azam, F., Tharazi, I., Bakar Sulong, A., Che Omar, R., Muhamad, N., 2024. Mechanical durability and degradation characteristics of long kenaf-reinforced PLA composites fabricated using an eco-friendly method. Eng. Sci. Technol., Int. J. 57. https://doi.org/10.1016/j.jestch.2024.101820.

Aguero, L., Alpdagtas, S., Ilhan, E., Zaldivar-Silva, D., Gunduz, O., 2021. Functional role of crosslinking in alginate scaffold for drug delivery and tissue engineering: A review. Eur. Polym. J. 160. https://doi.org/10.1016/j.eurpolymj.2021.110807.

Alshahrani, H., Prakash, V.R.A., 2024. Effect of silane-grafted orange peel biochar and areca fibre on mechanical, thermal conductivity and dielectric properties of epoxy resin composites. Biomass-.-. Convers. Biorefin 14, 8081–8089. https://doi.org/10.1007/s13399-022-02801-w.

Amin, M.T., Alazba, A.A., Shafiq, M., 2019. Comparative study for adsorption of methylene blue dye on biochar derived from orange peel and banana biomass in aqueous solutions. Environ. Monit. Assess. 191. https://doi.org/10.1007/s10661-019-7915-0.

Asthana, N., Khan, U.A., Srivastava, A., Kumar, D., Mishra, A.K., 2024. Integration and Characterization of Synthetic Biodegradable Polymer (PVA) with Graphite Oxide (GO) for Performance Assessment in Sustainable Electrochemical Devices. J. Inorg. Organomet Polym. Mater. https://doi.org/10.1007/s10904-024-03374-z.

Azka, M.A., Sapuan, S.M., Abral, H., Zainudin, E.S., Aziz, F.A., 2024. An examination of recent research of water absorption behavior of natural fiber reinforced polylactic acid (PLA) composites: A review. Int J. Biol. Macromol. https://doi.org/10.1016/j.ijbiomac.2024.131845.

Chen, Z., Lin, B., Huang, Y., Liu, Y., Wu, Y., Qu, R., Tang, C., 2023. Pyrolysis temperature affects the physiochemical characteristics of lanthanum-modified biochar derived from orange peels: Insights into the mechanisms of tetracycline adsorption by spectroscopic analysis and theoretical calculations. Sci. Total Environ. 862. https://doi.org/10.1016/j.scitotenv.2022.160860.

Choi, I., Lee, Y., Lyu, J.S., Lee, J.S., Han, J., 2022. Characterization of ionically crosslinked alginate films: Effect of different anion-based metal cations on the improvement of water-resistant properties. Food Hydrocoll. 131. https://doi.org/10.1016/j.foodhyd.2022.107785.

Dananjaya, S.A.V., Chevali, V.S., Dear, J.P., Potluri, P., Abeykoon, C., 2024. 3D printing of biodegradable polymers and their composites – Current state-of-the-art, properties, applications, and machine learning for potential future applications. Prog. Mater. Sci. https://doi.org/10.1016/j.pmatsci.2024.101336.

Díez-García, I., Lemma, M.R., de, C., Barud, H.S., Eceiza, A., Tercjak, A., 2020. Hydrogels based on waterborne poly(urethane-urea)s by physically cross-linking with sodium alginate and calcium chloride. Carbohydr. Polym. 250. https://doi.org/10.1016/j.carbpol.2020.116940.

Giz, A.S., Berberoglu, M., Bener, S., Aydelik-Ayazoglu, S., Bayraktar, H., Alaca, B.E., Catalgil-Giz, H., 2020. A detailed investigation of the effect of calcium crosslinking and glycerol plasticizing on the physical properties of alginate films. Int J. Biol. Macromol. 148, 49–55. https://doi.org/10.1016/j.ijbiomac.2020.01.103.

Hussain, M., Khan, S.M., Shafiq, M., Abbas, N., 2024. A review on PLA-based biodegradable materials for biomedical applications. Giant. https://doi.org/10.1016/j.giant.2024.100261.

Jin, X., Wu, C., Wang, H., Pan, Y., Huang, H., Wang, W., Fan, J., Yan, X., Hong, C., Zhang, X., 2023. Synergistic reinforcement and multiscaled design of lightweight heat protection and insulation integrated composite with outstanding high-temperature resistance up to 2500 °C. Compos Sci. Technol. 232. https://doi.org/10.1016/j.compscitech.2022.109878.

Khouri, N.G., Bahú, J.O., Blanco-Llamero, C., Severino, P., Concha, V.O.C., Souto, E.B., 2024. Polylactic acid (PLA): Properties, synthesis, and biomedical applications – A review of the literature. J. Mol. Struct. https://doi.org/10.1016/j.molstruc.2024.138243.

Krapež Tomec, D., Schwarzkopf, M., Repič, R., Žigon, J., Gospodarič, B., Kariž, M., 2024. Effect of thermal modification of wood particles for wood-PLA composites on properties of filaments, 3D-printed parts and injection moulded parts. Eur. J. Wood Wood Prod. 82, 403–416. https://doi.org/10.1007/s00107-023-02018-2.

Kwon, D., Oh, J.I., Lam, S.S., Moon, D.H., Kwon, E.E., 2019. Orange peel valorization by pyrolysis under the carbon dioxide environment. Bioresour. Technol. 285. https://doi.org/10.1016/j.biortech.2019.121356.

Li, S.Q., Tang, R.C., Yu, C.B., 2022. Flame retardant treatment of jute fabric with chitosan and sodium alginate. Polym. Degrad. Stab. 196. https://doi.org/10.1016/j.polymdegradstab.2022.109826.

Liesenfeld, J., Jablonski, J.J., da Silva, J.R.F., Buenos, A.A., Scheuer, C.J., 2024. Impact of annealing on the characteristics of 3D-printed graphene-reinforced PLA composite. J. Manuf. Process 128, 133–157. https://doi.org/10.1016/j.jmapro.2024.08.025.

Lule, Z.C., Kim, J., 2022. Surface treatment of lignocellulose biofiller for fabrication of sustainable polylactic acid biocomposite with high crystallinity and improved burning antidripping performance. Mater. Today Chem. 23. https://doi.org/10.1016/j.mtchem.2021.100741.

Moradi-Choghamarani, F., Moosavi, A.A., Baghernejad, M., 2019. Determining organo-chemical composition of sugarcane bagasse-derived biochar as a function of pyrolysis temperature using proximate and Fourier transform infrared analyses. J. Therm. Anal. Calor. 138, 331–342. https://doi.org/10.1007/s10973-019-08186-9.

Narukulla, R., Ojha, U., Sharma, T., 2022. Facile one pot green synthesis of –NH2 surface functionalized graphene-polymer nanocomposite: Subsequent utilization as stabilizer in pickering emulsions. Colloids Surf. A Physicochem Eng. Asp. 641. https://doi.org/10.1016/j.colsurfa.2022.128594.

Omura, T., Isobe, N., Miura, T., Ishii, S., Mori, M., Ishitani, Y., Kimura, S., Hidaka, K., Komiyama, K., Suzuki, M., Kasuya, K. ichi, Nomaki, H., Nakajima, R., Tsuchiya, M., Kawagucci, S., Mori, H., Nakayama, A., Kunioka, M., Kamino, K., Iwata, T., 2024. Microbial decomposition of biodegradable plastics on the deep-sea floor. Nat. Commun. 15. https://doi.org/10.1038/s41467-023-44368-8.

Praipipat, P., Ngamsurach, P., Joraleeprasert, T., 2023. Synthesis, characterization, and lead removal efficiency of orange peel powder and orange peel powder doped iron (III) oxide-hydroxide. Sci. Rep. 13. https://doi.org/10.1038/s41598-023-38035-7.

Raja, T., Devarajan, Y., 2024. A novel way of converting waste-enriched composites to lightweight, biodegradable resources: a property analysis. Biomass-.-. Convers. Biorefin 14, 19431–19441. https://doi.org/10.1007/s13399-023-03872-z.

Sial, T.A., Lan, Z., Khan, M.N., Zhao, Y., Kumbhar, F., Liu, J., Zhang, A., Hill, R.L., Lahori, A.H., Memon, M., 2019. Evaluation of orange peel waste and its biochar on greenhouse gas emissions and soil biochemical properties within a loess soil. Waste Manag. 87, 125–134. https://doi.org/10.1016/j.wasman.2019.01.042.

Song, Q., Ouyang, B., Lin, Y., Wang, C., 2023. Cross-linked sodium alginate-carboxymethyl chitosan hydrogel beads for adsorption of Ni(II) ions. Desalin. Water Treat. 286, 183–191. https://doi.org/10.5004/dwt.2023.29326.

Tan, J., Luo, Y., Guo, Y., Zhou, Y., Liao, X., Li, D., Lai, X., Liu, Y., 2023. Development of alginate-based hydrogels: Crosslinking strategies and biomedical applications. Int J. Biol. Macromol. https://doi.org/10.1016/j.ijbiomac.2023.124275.

Tang, W., Luo, L., Chen, Y., Li, J., Dai, Y., Xie, Y., Ma, Y., Zhang, J., Zhang, Y., 2025. Noble-metal-free Bi-OZIS nanohybrids for sacrificial-agent-free photocatalytic water splitting: With long-lived photogenerated electrons. Sep Purif. Technol. 357. https://doi.org/10.1016/j.seppur.2024.130047.

Terzioğlu, P., Güney, F., Parın, F.N., Şen, İ., Tuna, S., 2021. Biowaste orange peel incorporated chitosan/polyvinyl alcohol composite films for food packaging applications. Food Packag Shelf Life 30. https://doi.org/10.1016/j.fpsl.2021.100742.

Urquiza, T.K.V., Pérez, O.P., Saldaña, M.G., 2011. Effect of the cross-linking with calcium ions on the structural and thermo-mechanical properties of alginate films, in: Materials Research Society Symposium Proceedings. pp. 16–21. https://doi.org/10.1557/opl.2011.1136.

Wang, F., Wu, P., Shu, L., Huang, D., Liu, H., 2022. High-efficiency adsorption of Cd(II) and Co(II) by ethylenediaminetetraacetic dianhydride-modified orange peel as a novel synthesized adsorbent. Environ. Sci. Pollut. Res. 29, 25748–25758. https://doi.org/10.1007/s11356-021-17501-7.

Wang, L., Zhang, H.J., Liu, Xueqian, Liu, Y., Zhu, X., Liu, Xinhua, You, X., 2021. A Physically Cross-Linked Sodium Alginate-Gelatin Hydrogel with High Mechanical Strength. ACS Appl. Polym. Mater. 3, 3197–3205. https://doi.org/10.1021/acsapm.1c00404.

Wu, K., Ye, Z., Cheng, J., Zeng, Y., Wang, R., Sun, W., Kuang, Y., Jiang, F., Chen, S., Zhao, X., 2023. Excellent thermal insulation and flame retardancy property of konjac glucomannan/sodium alginate aerogel reinforced by phytic acid. Ind. Crops Prod. 205. https://doi.org/10.1016/j.indcrop.2023.117495.

Xiang, X., Yi, X., Zheng, W., Li, Y., Zhang, C., Wang, X., Chen, Z., Huang, M., Ying, G.G., 2023. Enhanced biodegradation of thiamethoxam with a novel polyvinyl alcohol (PVA)/sodium alginate (SA)/biochar immobilized Chryseobacterium sp H5. J. Hazard Mater. 443. https://doi.org/10.1016/j.jhazmat.2022.130247.

Xu, P., Song, J., Dai, Z., Xu, Y., Li, D., Wu, C., 2021. Effect of Ca2+ cross-linking on the properties and structure of lutein-loaded sodium alginate hydrogels. Int J. Biol. Macromol. 193, 53–63. https://doi.org/10.1016/j.ijbiomac.2021.10.114.

Xue, Y., Kamali, M., Aminabhavi, T.M., Appels, L., Dewil, R., 2024. Tailoring the surface functional groups of biochar for enhanced adsorption and degradation of pharmaceutically active compounds. Chem. Eng. J. 491. https://doi.org/10.1016/j.cej.2024.152037.

Yan, M., Cheng, X., Gong, L., Lun, Z., He, P., Shi, L., Liu, C., Pan, Y., 2023. Growth mechanism and structure regulation of super-elastic SiC aerogels for thermal insulation and electromagnetic wave absorption. Chem. Eng. J. 475. https://doi.org/10.1016/j.cej.2023.146417.

Yu, J., Wang, Y., He, Y., Gao, Y., Hou, R., Ma, J., Zhang, L., Guo, X., Chen, L., 2021. Calcium ion-sodium alginate double cross-linked graphene oxide nanofiltration membrane with enhanced stability for efficient separation of dyes. Sep Purif. Technol. 276. https://doi.org/10.1016/j.seppur.2021.119348.

Zhang, C., Hu, Y., Shao, J., Pan, H., 2023. Flame retardant cellulose/polyvinyl alcohol/sodium alginate composite aerogels crosslinked by metal ions for flame resistance materials. Cellulose 30, 7079–7093. https://doi.org/10.1007/s10570-023-05277-7.

Zhang, Y., Zhu, M., Huang, Z., Yang, F., Weng, Y., Zhang, C., 2024. The effect of polylactic acid-based blend films modified with various biodegradable polymers on the preservation of strawberries. Food Packag Shelf Life 45. https://doi.org/10.1016/j.fpsl.2024.101333.

Zhao, X., Liu, J., Li, J., Liang, X., Zhou, W., Peng, S., 2022. Strategies and techniques for improving heat resistance and mechanical performances of poly(lactic acid) (PLA) biodegradable materials. Int J. Biol. Macromol. https://doi.org/10.1016/j.ijbiomac.2022.07.091.

Zheng, H., Yang, J., Han, S., 2016. The synthesis and characteristics of sodium alginate/graphene oxide composite films crosslinked with multivalent cations. J. Appl. Polym. Sci. 133. https://doi.org/10.1002/app.43616.

Zhou, X.W., Huang, J., Zhang, X.H., Li, T., Wang, Y., Wang, S.B., Xia, B.H., Dong, W.F., 2023. Design of Tough, yet Strong, Heat-resistant PLA/PBAT Blends with Reconfigurable Shape Memory Behavior by Engineering Exchangeable Covalent Crosslinks. Chin. J. Polym. Sci. (Engl. Ed. ) 41, 1868–1878. https://doi.org/10.1007/s10118-023-2997-0.